Journal of Materials Science & Technology 194 (2024) 180–184

Contents lists available at ScienceDirect

Journal of Materials Science & Technology

journal homepage: www.elsevier.com/locate/jmst

Letter

Development of a superb degradable lightweight Mg alloy with high compressive strength

1. Introduction

Hydraulic fracturing is a cost-effective method that can significantly increase unconventional oil and gas production from the reservoir with low porosity and permeability. The fracturing tools, such as bridge plug and fracturing ball, are crucial components used in hydraulic fracturing to seal oil and gas wells temporarily. During fracturing, the fracturing tools are first sent to the downhole with wellbore fluid. Using lightweight materials makes the sent process easier and benefits the settling process [1,2]. Then the tools are used to seal the pipes and endure high liquid pressure to create downhole cracks, thus requiring the candidate materials with high compressive strength (more than 450 MPa in ultrahigh hydraulic pressure operations [1]). Once the fracturing process finishes, the fracturing tools need to be removed to open the pathway for oil and gas flow. Traditional fracturing tools, usually made of mild steel, phenolic, and polyether ether ketone (PEEK), which are non-degradable materials, require costly and time-consuming mechanical milling, posing a risk of underground accidents and contamination of oil and gas reservoirs [3,4]. In contrast, fracturing tools made by degradable Mg alloys can self-degrade after fracturing in flow back water that contains chloride ions, which no longer requires mechanical milling. Therefore, degradable Mg alloys are attractive for manufacturing fracturing tools in unconventional oil and gas extraction and have been widely studied in recent years [5–15]. However, in some extreme downhole environments with low temperatures and low chloride ion concentrations, the degradation rate of common Mg alloys is still insufficient. Consequently, it is important to develop lightweight Mg alloys with better degradation rates and high compressive strength.

One common strategy for designing highly degradable Mg alloys for fracturing tools is to directly add high-potential elements like Ni (−0.25 V vs. SHE (Standard Hydrogen Electrode)) and Cu (0.159 V vs. SHE) elements to existing Mg alloys to form Ni, Cu-containing second phases to promote galvanic corrosion [5,7–34]. Mg-Al, Mg-Zn, and Mg-RE alloys are commonly chosen because these alloys usually have high strength. However, the solid solution of Al, Zn, and RE elements in these alloys can increase the potential of the anodic matrix and decrease the potential difference of the corrosion couples, thus decreasing the degradation rate. Table 1 summarizes the reported potential difference between the Ni, Cu-containing second phases and Mg matrix in degradable Mg alloys. For example, in Mg-8Gd-3.5Cu and Mg-2Gd-1Cu alloys, the potential difference between (α-Mg) and Mg_2Cu is only 186 [35] and 225 mV [36], respectively, which are much lower than the potential difference between pure Mg and Mg_2Cu, i.e., 417 mV [37]. That is, the solid solution of Gd to Mg matrix increases the anodic matrix potential, thus decreasing the potential difference between Mg_2Cu and Mg matrix, which weakens the galvanic corrosion.

In this work, a lightweight Mg-Li-Ni-Cu alloy with a superb degradation rate and high compressive strength was designed and manufactured. Mg-Li system is chosen because the potential of Li is lower than that of Mg. Consequently, the solid solution of Li will decrease the anodic matrix potential, which increases the potential difference of the galvanic couple. Meanwhile, the addition of Li can reduce the alloy density. The added Ni and Cu can form Ni/Cu-containing second phases with Mg, which has a high Volta potential. At the same time, the Ni and Cu can also refine the grain size to guarantee high strength.

2. Materials and experiments

The alloy with a nominal composition of Mg-4Li-0.5Cu-6Ni (wt.%) was prepared through casting with argon protection and extrusion (300 ± 5 °C, extrusion ratio of 18:1 at a rate of 0.2 mm/s). The density of the alloys was evaluated using the Archimedes method on six samples with absolute ethylalcohol as a suspending medium (Analytical Balance, GT204, China). The samples were precisely weighted to an accuracy of 10^{-4} g. The chemical composition was determined by an inductively coupled plasma (ICP) emission spectrometer (Table 2). Microstructural features were characterized using optical microscopy (OM), scanning electron microscopy (SEM), and transmission electron microscopy (TEM) coupled with an energy-dispersive spectrometer (EDS). Crystal structures were determined by X-ray diffraction (XRD). The Volta potential was measured by an AFM (SPM-9700HT) using scanning Kelvin probe microscopy (SKPM) mode. The corrosion rate was measured by two methods, pH (hydrogen evolution rate) and P_W (weight loss rate), which was then converted to average corrosion rate (mm/y) using the standard of ASTM G31-72. The potentiodynamic polarization curve was tested from catholic −0.2 V (E_{OCP}) to anodic 0.2 V (E_{OCP}) with a scan rate of 0.5 mV/s by using an electrochemical workstation (VersaSTAT 3F, Princeton Applied Research). Tafel extrapolation from the cathodic branch evaluates corrosion potential (E_{corr}) and corrosion current density (i_{corr}). The EIS was obtained in the range of 10^5–10^{-2} Hz with an AC amplitude of 10 mV. The potentiodynamic polarization curves were tested from catholic −0.2 V (E_{OCP}) to anodic 0.2 V (E_{OCP}) with a scan rate of 1 mV/s. Surface chemistry of specimens, subjected to 1 h immersion in 3.0 wt.% KCl solution at room temperature, was analyzed by X-ray photoelectron spectroscopy (XPS, ESCALAB Xi+, Thermo Fisher). The binding energy values were calibrated by the C 1s (hydrocarbon C–C) of 284.8 eV. Compression and tensile tests were performed on the Gleeble 3800 and Instron 5969 testing machines, respectively. All tests were conducted along the extrusion direction (ED) on a strain rate of 10^{-3} s^{-1} at room temperature.

https://doi.org/10.1016/j.jmst.2023.12.073

Table 1
Reported potential differences between the Ni, Cu-containing second phases and Mg matrix from literature.

Galvanic couple	Potential difference (mV)	Alloy composition
(α-Mg)-Mg_5(Gd, Cu)	75	Mg-8Gd-3.5Cu [35]
(α-Mg)-(Cu-containing SF)	64–85	
(α-Mg)-Mg_2Cu	186	
(α-Mg)-Mg_2Cu	225	Mg-2Gd-1Cu [36]
(α-Mg)-(Cu-containing block LPSO)	155	Mg-9.5Gd-2.7Y-0.9Zn-0.4Cu [32]
(α-Mg)-(Cu-containing plate LPSO)	80	
Mg-Mg_2Cu	430	Mg-2.5Cu-(4, 5, 6 wt.%) Al [16]
(α-Mg)-MgAlCu	540	
(α-Mg)-Al_2Cu	230	
(α-Mg)-Zr_7Ni_{10}	–40	Mg-10Gd-3Y-0.3Zr-(0.2, 0.4, 0.6 wt.%) Ni [10]
(α-Mg)-Ni containing LPSO	170	
(α-Mg)-(Ni, Cu-containing lamellar LPSO)	110	Mg-9.5Gd-2.7Y-0.9Zn-0.8Cu-0.4Ni [12]
(α-Mg)-(Ni, Cu-containing block LPSO)	170	

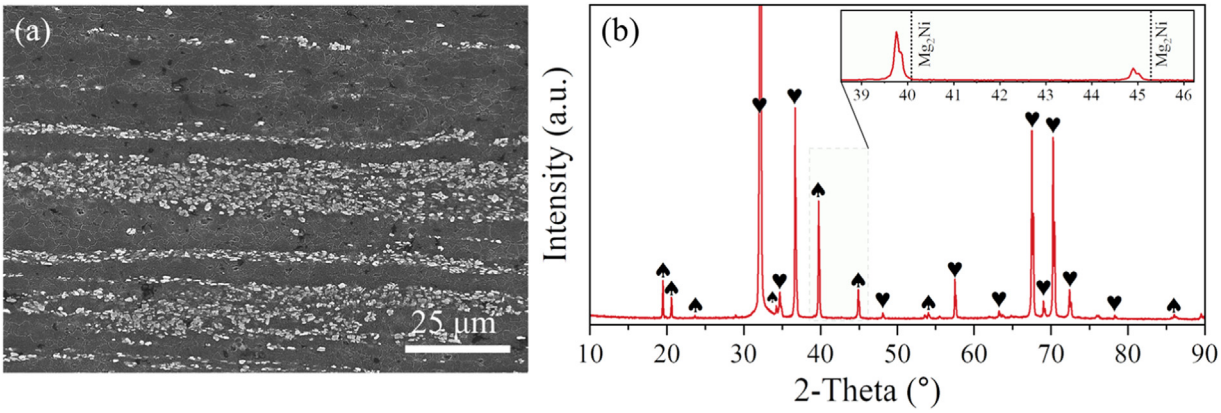

Fig. 1. SEM and X-ray diffraction characterizations of the second phases. (a) SEM results show a large amount of second phases (10.0 ± 0.2 vol.%) that distribute along the extrusion direction. (b) XRD shows the diffraction peaks of the second phase that are close to Mg_2Ni. The inset magnified pattern shows that the peak slightly shifts left to the theoretical value of Mg_2Ni.

Table 2
Chemical composition of the designed Mg alloy (wt.%).

Samples	Ni	Li	Cu	Mg
Mg-4Li-0.5Cu-6Ni	6.28	3.71	0.50	Bal.

3. Results and discussion

SEM characterizations demonstrate that a large number of second phases was formed in the as-extruded alloy, with a volume fraction of 10.0% ± 0.2%, distributed along the extrusion direction (Fig. S1(a) in the Supplementary Material). The XRD result shows that the diffraction peaks of the second phase are close to that of Mg_2Ni, but the peak slightly shifted left to the theoretical value of Mg_2Ni (Fig. 1(b)), which is usually due to lattice distortion caused by atomic substitution. TEM characterization of the second phase shows that the diffraction pattern of the second phase was consistent with that of Mg_2Ni (Fig. 2(a–c)). EDS mapping results (Figs. 2(d) and S1 and S2) reveal that the second phase contains Mg, Ni, and Cu elements. The above results suggest the formation of second phases with crystal structure of Mg_2Ni and some of the Ni atoms were replaced by Cu atoms. Similar structures can also be found in other Refs. [38,39]. According to its crystal structure and composition, such second phase is termed as Mg_2(Ni, Cu) hereinafter. Most grains of the prepared alloy are equiaxed, indicating that dynamic recrystallization occurs during hot extrusion (Fig. 1(a)). Statistically, the average grain size is ~1.50 μm (Fig. S3), which is expected to provide a significant grain refinement strengthening.

Composition analysis of the corrosion product film reveals that only $Mg(OH)_2$ and MgO are formed on the surface of the Mg matrix (Fig. S4). It is well known that the formed $Mg(OH)_2$/MgO film does not effectively protect the Mg matrix, in this situation, the degradation of Mg alloys mainly depends on the potential difference of formed corrosion couples [48,49]. The formed Mg_2(Ni, Cu) second phase exhibits a very large potential difference to the Mg-Li matrix (Fig. 3). The sample was electropolished and used to perform surface morphology and potential tests. Surface morphology mapping shows that the height of Mg_2(Ni, Cu) phase was higher than that of the matrix (Fig. 3(a)), indicating that the matrix part was corroded in a much faster manner than the second phases during electropolishing. Volta-potential mapping, as well as the line scanning analysis, demonstrates that the area with higher potential coincides with the higher area, which means that these residual second phases have higher potential than the matrix (Fig. 3(b, c)). This indicates that galvanic corrosion occurred during the electropolish, i.e., the high potential Mg_2(Ni, Cu) phase acts as cathode and the low potential Mg-Li matrix corrodes as anode. The Volta-potential difference of the Mg_2(Ni, Cu) phase and matrix is 500 ± 21 mV, which far exceeds most of the corrosion couples in Table 1.

The largely formed Mg_2(Ni, Cu) phases with high potential difference to the Mg-Li matrix serve as numerous high-efficient corrosion couples, suggesting a superb degradation rate, which was then verified by immersion tests. The degradation rate was quantified by hydrogen evolution (pH) and weight loss (P_W) in 3.0 wt.% KCl solution at room temperature (Figs. 4(a) and S5). The pH and P_W of the designed alloy are 2252.3 and 2404.3 mm/y, respectively, which is much higher than the reported highest degradation rate of extruded Mg alloy fracturing tools (P_W, 1056.8 mm/y).

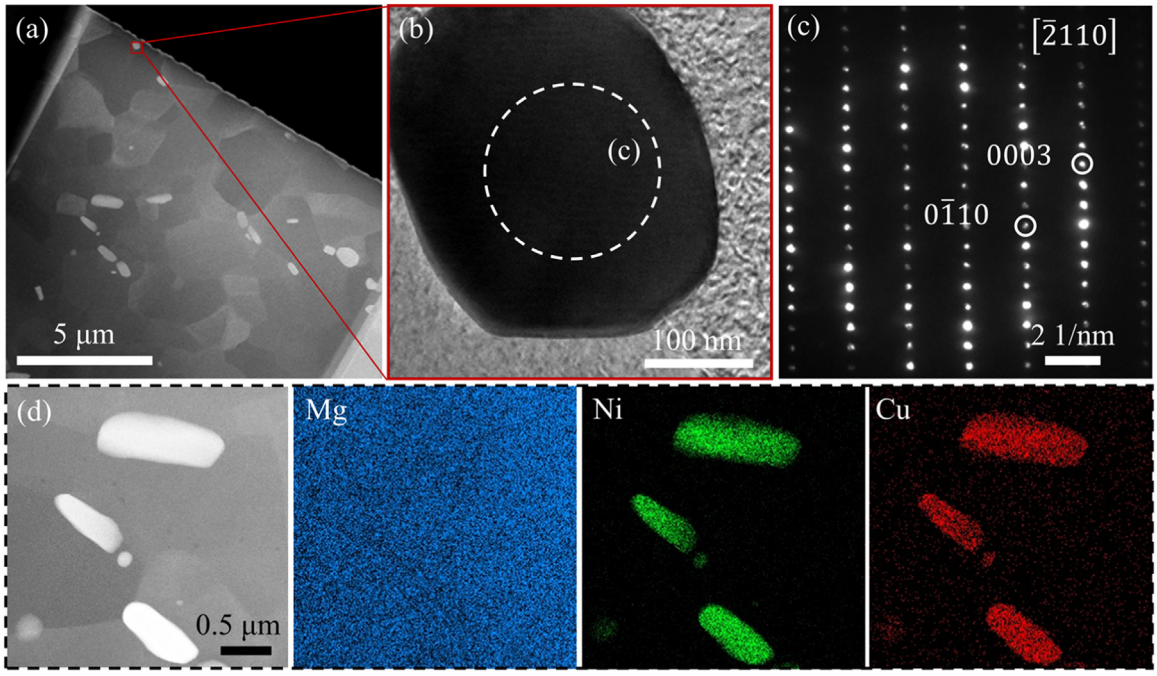

Fig. 2. STEM, TEM, and EDS characterization shows that the second phase mainly comprises Mg, Ni, and Cu and has a similar crystal structure of Mg_2Ni. (a) STEM bright field images show that the second phases distribute along the grain boundaries; (b, c) A typical second phase and corresponding selected area electron diffraction (SAED) result, which is consistent with the pattern of Mg_2Ni under the same viewing direction; (d) EDS mapping shows that the second phase is composed of Mg, Ni, and Cu.

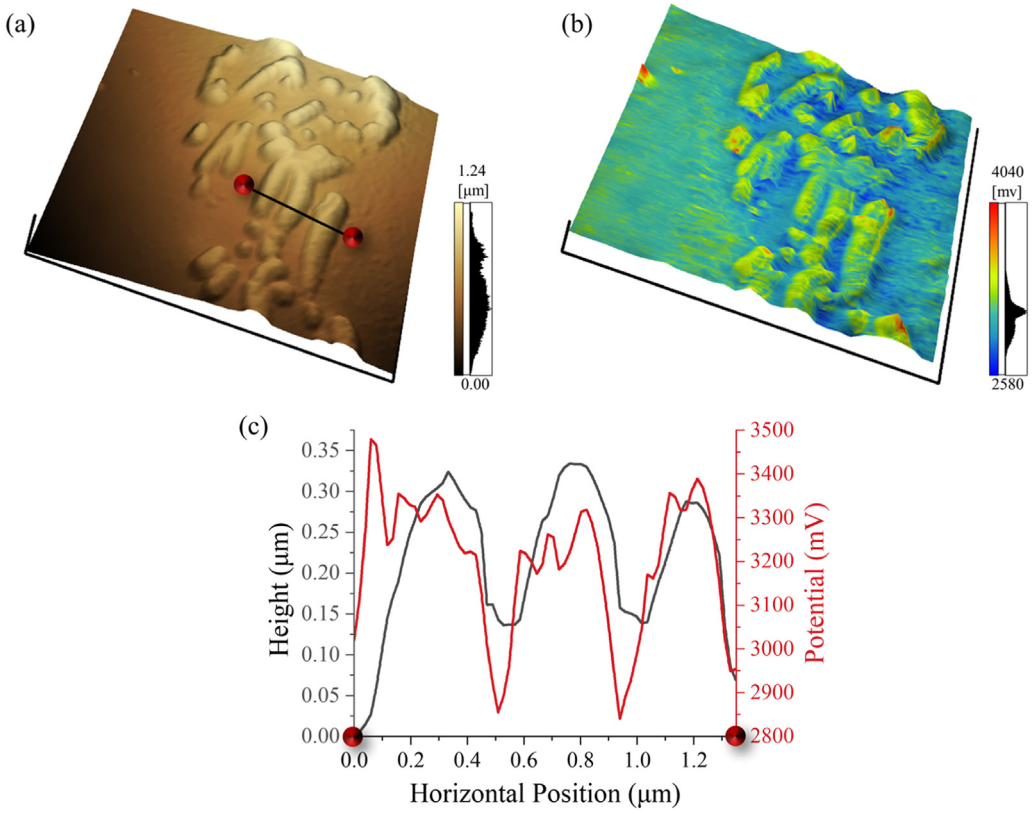

Fig. 3. Surface morphology (a), potential mapping (b), and line scan (c) show that the second phases have high potential compared with the Mg-Li matrix and remains after electropolishing, indicating the occurrence of galvanic corrosion, where the second phase acts as cathode and Mg-Li matrix corrodes as the anode. The line scan is conducted the black line marked in (a).

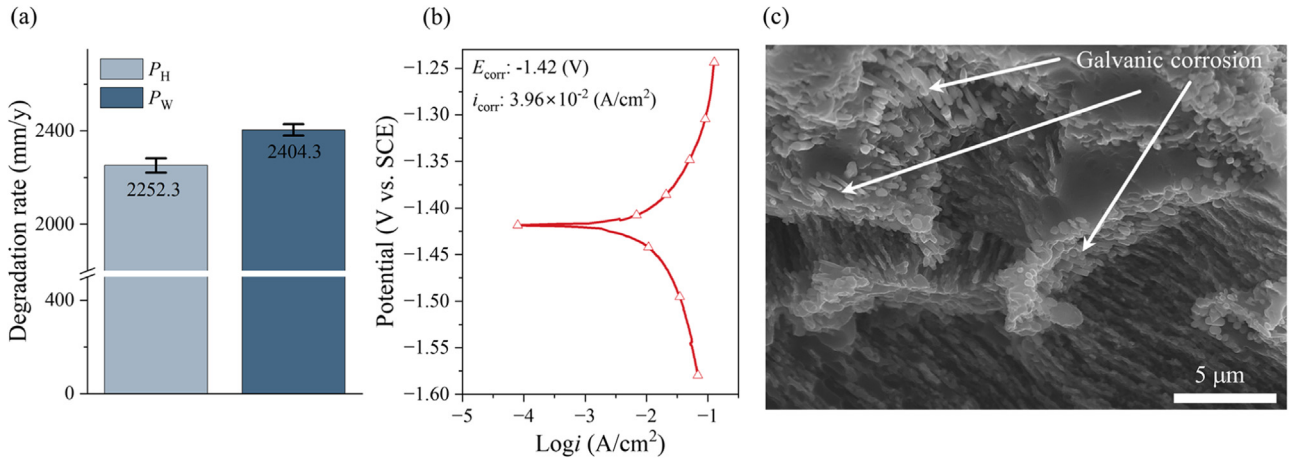

Fig. 4. Corrosion experiments show that the designed alloy has a high degradation rate caused by intense galvanic corrosion. (a) degradation rates measured by hydrogen evolution (pH) and weight loss (P_W) experiments, (b) potentiodynamic polarization curve, (c) SEM observation of specimen surface shows that second phases remained after corrosion, indicating galvanic corrosion.

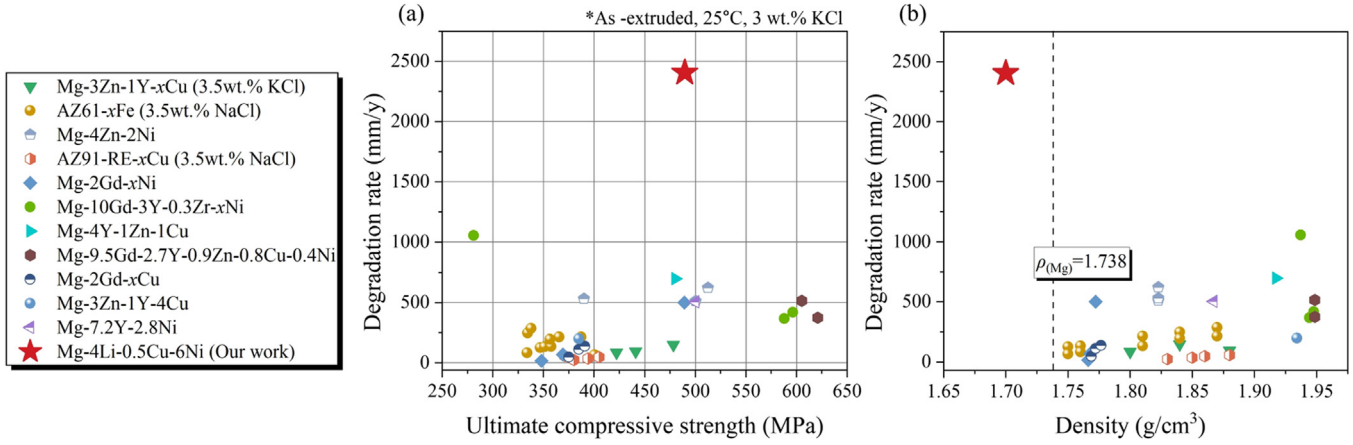

Fig. 5. The designed alloy exhibits a superb degradation rate, relatively high compressive strength (a), and lower density (b) compared to other extruded degradable Mg alloys for fracturing tools. The figure was drawn based on the results of this work and Refs. [5–15]. For those alloys their densities were not directly provided in the literature, we used Factsage to estimate their densities.

The charge transfer resistance (R_a) and corrosion product resistance (R_f) values are only 0.57 and 4.09 (Fig. S6 and Table S1), which indicates an activated matrix that fails to form an effective protective film. Fig. 4(b) shows the potentiodynamic polarization curve of the designed alloy. The i_{corr} is 3.96 × 10^{-2} A/cm^2, which is much higher than those of the reported i_{corr} of extruded Mg alloys for fracturing tools (in the range of 1.78 × 10^{-6} to 1.20 × 10^{-3} A/cm^2 [5–15]). Numerous short rods of Mg_2(Ni, Cu) phases were observed on the corroded sample surface after the immersion test (Figs. 4(c) and S7), which further confirmed the strong galvanic corrosion.

According to the compressive curve (Fig. S8), the alloy has high compressive strength (484.9 ± 7.9 MPa) and plasticity (compressive strain before fracture of about 16.1% ± 0.1%), which can be attributed mainly to its fine grain size. Furthermore, the solution of Li also can increase the activity of ⟨c + a⟩ slip to improve the plasticity (Fig. S9). The average grain size of the designed alloy is about 1.5 μm, smaller than the typical grain size of extruded Mg-Li-based alloys with HCP structure (in the range of 1.5–35 μm [40–46]). The grain refinement is caused by the addition of Ni and Cu with high grain restriction factor (Ni-6.13, Cu-5.28) [47] that can refine the grains during solidification. Moreover, the generated Mg_2(Ni, Cu) phases can further inhibit grain boundary migration thus restricting the grain growth during hot extrusion.

Fig. 5 compares the compressive strength, degradation rate, and density of the Mg-Li-Cu-Ni alloy and other extruded Mg alloys designed for fracturing tools [5–15]. The designed Mg-Li-Cu-Ni alloy has a superb degradation rate (2404.3 mm/y), 3.6–16.2 times higher than that of other competitive Mg alloys. At the same time, the alloy has a relatively high compressive strength (484.9 MPa) that satisfies the requirement in ultrahigh hydraulic pressure operations [1]. Moreover, the density of the Mg-Li-Cu-Ni alloy is only 1.70 g/cm^3, lower than the density of existing degradable Mg alloys for fracturing tools (1.75–1.95 g/cm^3), making the sent process easier. It can be seen that the designed alloy has a competitive advantage over other comparative Mg alloys in the literature. In addition, a 3–5 day pause is generally needed for tools to complete degradation after fracturing (data from SJS Petroleum Drilling & Production Equipment Co., Ltd.). The employment of high degradation rate Mg alloys in this study can shorten pause time and reduce costs, especially in extreme downhole conditions (low temperature, low chloride ion concentrations), which indicates that this work is sufficiently practical.

4. Conclusion

In summary, the present work designed a superb degradable Mg alloy with high compressive strength and low density. The Mg-Li system was selected to decrease the anodic matrix poten-

tial. Combined by introducing high potential Mg_2(Ni, Cu) phases, a large number of galvanic couples with high potential differences ((α-Mg)-Mg_2(Ni, Cu)) formed, leading to an ultrahigh degradation rate. The Mg-Li matrix also enables low density. Moreover, adding Ni and Cu and the formation of the Mg_2(Ni, Cu) phase can refine the grains (1.5 μm), leading to high strength and plasticity. The designed Mg alloy is expected to meet the increasing demand for higher performance in harsh downhole environments, such as low temperature, low chloride concentrations, and ultrahigh hydraulic pressure operations.

Declaration of competing interest

We declare that we have no financial and personal relationships with other people or organizations that can inappropriately influence our work, there is no professional or other personal interest of any nature or kind in any product, service and/or company that could be construed as influencing the position presented in, or the review of, the manuscript entitled “Development of a superb degradable lightweight Mg alloy with high compressive strength”.

Acknowledgments

The authors gratefully acknowledge the support of the National Key Research and Development Program of China (No. 2022YFB3709300), National Natural Science Foundation of China (Nos. 52031011, 52371121, 51971168, and 52022076), Shaanxi Province Science and Technology Department Project (No. 2021GXLH-Z-015). We thank Yao-Feng Li, Chuan-Wei Fan, Zi-Jun Ren, and Chang-Bo Yi from Xi’an Jiaotong University for their assistance with the TEM experiments, mechanical test, AFM analysis, and degradation rate test, respectively. We give special thanks to Xiao-Cheng Yang (SJS Petroleum Drilling & Production Equipment Co., Ltd.) for discussions about the applications and requirements of degradable Mg alloys used for fracturing tools.

Supplementary materials

Supplementary material associated with this article can be found, in the online version, at doi:10.1016/j.jmst.2023.12.073.

References

[1] Z. Xu, B.M. Richard, M.D. Solfronk, All Days, IPTC, Beijing, China, 2013, IPTC-16538-MS.
[2] L. Liu, S. Yu, E. Liu, G. Zhu, Q. Li, W. Xiong, B. Wang, X. Yang, Adv. Eng. Mater. 23 (2021) 2100615.
[3] X. Li, Q. Yu, X. Chen, Q. Zhang, J. Magnes. Alloy. 11 (2023) 1213–1223.
[4] L. Liu, S. Yu, E. Liu, Y. Zhao, B. Wang, Y. Niu, J. Alloy. Compd. 853 (2021) 157125.
[5] B. Liu, Y. Kuang, D. Fang, Y. Chai, Y. Zhang, Int. J. Mater. Res. 108 (2017) 262–268.
[6] C. Zhang, L. Wu, G. Huang, L. Chen, D. Xia, B. Jiang, A. Atrens, F. Pan, J. Mater. Sci. Technol. 35 (2019) 2086–2098.
[7] H. Niu, K. Deng, K. Nie, C. Wang, W. Liang, Y. Wu, Mater. Chem. Phys. 249 (2020) 123131.
[8] B. Liu, Y. Yang, Y. Zhang, H. Du, L. Hou, Y. Wei, J. Phys. Chem. Solids 144 (2020) 109499.
[9] Y. Wang, D. Zhang, S. Zhong, Q. Dai, J. Hua, Y. Luo, G. Hu, J. Xu, B. Jiang, F. Pan, J. Mater. Res. Technol. 20 (2022) 3735–3749.
[10] J. Wang, T. Li, H.X. Li, Y.Z. Ma, K.N. Zhao, C.L. Yang, J.S. Zhang, J. Magnes. Alloy. 9 (2021) 1632–1643.
[11] B. Liu, G. Dong, X. Ren, Y. Zhang, Y. Wei, Int. J. Mater. Res. 111 (2020) 872–875.
[12] Y.H. Liu, Z.R. Zhang, J. Wang, Y. Li, H.X. Li, L.Y. Jia, J.H. Wang, J.S. Zhang, J. Magnes. Alloy. 11 (2023) 720–734.
[13] S. Zhong, D. Zhang, S. Chai, J. Zhou, J. Hua, J. Xu, B. Jiang, F. Pan, J. Mater. Res. Technol. 15 (2021) 477–487.
[14] Y. Zhang, X. Wang, Y. Kuang, B. Liu, K. Zhang, D. Fang, Mater. Lett. 195 (2017) 194–197.
[15] K. Ma, J. Wang, J. Ren, C. Dai, S. Liu, Y. Peng, Y. Pan, Mater. Charact. 181 (2021) 111489.
[16] W. Tan, T. Li, S. Li, D. Fang, X. Ding, J. Sun, J. Mater. Sci. Technol. 94 (2021) 22–31.
[17] D.H. Xiao, Z.W. Geng, L. Chen, Z. Wu, H.Y. Diao, M. Song, P.F. Zhou, Metall. Mater. Trans. A 46 (2015) 4793–4803.
[18] M. Zhou, C. Liu, S. Xu, Y. Gao, S. Jiang, Mater. Corros. 69 (2018) 760–769.
[19] L. Chen, Z. Wu, D.H. Xiao, Z.W. Geng, P.F. Zhou, Mater. Corros. 66 (2015) 1159–1168.
[20] X.W. Wang, W. Wang, W. Chen, D.M. Chen, J. Mater. Sci. Technol. 98 (2022) 219–232.
[21] X.W. Wang, W. Wang, W. Chen, D.M. Chen, Mater. Charact. 177 (2021) 111157.
[22] Z. Geng, D. Xiao, L. Chen, J. Alloy. Compd. 686 (2016) 145–152.
[23] M.F. Wang, D.H. Xiao, P.F. Zhou, W.S. Liu, Y.Z. Ma, B.R. Sun, J. Alloy. Compd. 742 (2018) 232–239.
[24] M. Wang, D.H. Xiao, W.S. Liu, Vacuum 141 (2017) 144–151.
[25] D. Wang, K. Dong, Z. Jin, K. Guan, F. Cao, H. Zhao, M. Zha, H.Y. Wang, J. Alloy. Compd. 914 (2022) 165325.
[26] H. Niu, K. Deng, K. Nie, F. Cao, X. Zhang, W. Li, J. Alloy. Compd. 787 (2019) 1290–1300.
[27] J. Wang, S. Gao, X. Liu, X. Peng, K. Wang, S. Liu, W. Jiang, S. Guo, F. Pan, J. Magnes. Alloy. 8 (2020) 127–133.
[28] S. Zhong, D. Zhang, Y. Wang, S. Chai, J. Feng, Y. Luo, J. Hua, Q. Dai, G. Hu, J. Xu, B. Jiang, F. Pan, J. Mater. Sci. Technol. 128 (2022) 44–58.
[29] Z. Han, K. Zhang, J. Yang, R. Wei, C. Zhang, Mater. Corros. 70 (2019) 537–548.
[30] K. Ma, S. Liu, C. Dai, X. Liu, J. Ren, Y. Pan, Y. Peng, C. Su, J. Wang, F. Pan, J. Mater. Sci. Technol. 91 (2021) 121–133.
[31] K. Ma, J. Wang, Y. Peng, C. Dai, Y. Pan, D. Wang, Y. Wang, S. Pei, Y. Ma, J. Phys. Chem. Solids 171 (2022) 110974.
[32] Y. Liu, H. Li, Z. Zhang, Y. Li, L. Jia, J. Wang, J. Wang, J. Zhang, J. Alloy. Compd. 939 (2023) 168768.
[33] C. Dai, S. Pei, K. Ma, Y. Wang, D. Wang, J. Wang, Y. Ma, J. Wang, J. Mater. Res. Technol. 24 (2023) 6246–6263.
[34] C. Dai, J. Wang, Y. Pan, K. Ma, Y. Peng, Y. Wang, D. Wang, C. Ran, J. Wang, Y. Ma, Corros. Sci. 220 (2023) 111227.
[35] K. Ma, J. Wang, W. Zheng, Y. Peng, C. Dai, Y. Pan, Y. Wang, D. Wang, J. Wang, Y. Ma, Corros. Sci. 208 (2022) 110689.
[36] S. Zhong, D. Zhang, J. Xu, J. Zhou, Y. Zhao, J. Feng, Y. Wang, B. Jiang, F. Pan, J. Electrochem. Soc. 168 (2021) 071504.
[37] K. Kondoh, R. Takei, S. Kariya, S. Li, J. Umeda, Mater. Chem. Phys. 279 (2022) 125760.
[38] X. Ding, R. Chen, X. Chen, W. Cao, Y. Su, H. Ding, J. Guo, Renew. Energy 166 (2020) 81–90.
[39] Y. Lv, B. Zhang, Y. Wu, J. Alloy. Compd. 645 (2015) S423–S427.
[40] G. Zhou, Y. Yang, L. Sun, J. Liu, H. Deng, C. Wen, G. Wei, B. Jiang, X. Peng, F. Pan, J. Mater. Res. Technol. 19 (2022) 4197–4208.
[41] T. Wang, R. Wu, M. Zhang, L. Li, J. Zhang, J. Li, Mater. Sci. Eng. A 528 (2011) 5678–5684.
[42] X. Li, C. Cheng, Q. Le, X. Zhou, Q. Liao, X. Chen, Y. Jia, P. Wang, J. Alloy. Compd. 805 (2019) 947–956.
[43] X. Li, Q. Le, X. Zhou, C. Cheng, Y. Cao, X. Chen, P. Wang, L. Ren, D. Li, Compos. Pt. B-Eng. 216 (2021) 108866.
[44] B. Jiang, H. Yin, Q. Yang, R. Li, F. Pan, Trans. Nonferrous Met. Soc. China 21 (2011) 2378–2383.
[45] Y. Sun, R. Wang, C. Peng, Y. Feng, Mater. Sci. Eng. A 733 (2018) 429–439.
[46] J. Li, Z. Qu, R. Wu, M. Zhang, J. Zhang, Mater. Sci. Eng. A 528 (2011) 3915–3920.
[47] E. Karakulak, J. Magnes. Alloy. 7 (2019) 355–369.
[48] P. Zhao, T. Ying, F. Cao, X. Zeng, W. Ding, J. Magnes. Alloy. 11 (2023) 3120–3129.
[49] X. Ma, S. Jin, R. Wu, J. Wang, G. Wang, B. Krit, S. Betsofen, Trans. Nonferrous Met. Soc. China 31 (2021) 3228–3254.

Zhang Liu
Shao-Chuan Zheng
Bo-Yu Liu*
Ming Liu
Dong-Lang Chai
Zhi-Wei Shan*
Engineering Research Center for Magnesium-Based New Materials, Center for Advancing Materials Performance from the Nanoscale (CAMP-Nano), State Key Laboratory for Mechanical Behavior of Materials, Xi’an Jiaotong University, Xi’an 710049, China
*Corresponding authors.
E-mail addresses: boyuliu@xjtu.edu.cn (B.-Y. Liu), zwshan@xjtu.edu.cn (Z.-W. Shan)
Revised 31 December 2023